

Machine Learning Time Propagators for Time-Dependent Density Functional Theory Simulations

Karan Shah^{1,2}, Attila Cangi^{1,2,*},

¹ Center for Advanced Systems Understanding, 02826 Görlitz, Germany

² Helmholtz-Zentrum Dresden-Rossendorf, 01328 Dresden, Germany

* a.cangi@hzdr.de

25 August 2025

Abstract. Time-dependent density functional theory (TDDFT) is a widely used method to investigate electron dynamics under external time-dependent perturbations such as laser fields. In this work, we present a novel approach to accelerate electron dynamics simulations based on real time TDDFT using autoregressive neural operators as time-propagators for the electron density. By leveraging physics-informed constraints and featurization, and high-resolution training data, our model achieves superior accuracy and computational speed compared to traditional numerical solvers. We demonstrate the effectiveness of our model on a class of one-dimensional diatomic molecules under the influence of a range of laser parameters. This method has potential in enabling real-time, on-the-fly modeling of laser-irradiated molecules and materials with varying experimental parameters.

1. Introduction

Time-Dependent Density Functional Theory (TDDFT) [1] is a widely used method to study the evolution of electronic structure under the influence of external time-dependent potentials. It is used to calculate various excited state properties such as excitation energies [2], charge transfer [3], stopping power [4], optical absorption spectra [5] and non-linear optical properties [6]. Due to its favorable balance between accuracy and computational cost, TDDFT has been applied in various domains including photocatalysis [7], biochemistry [8], nanoscale devices [9] and the study of light-matter interactions in general [10].

For weak perturbations, the linear response (LR) formalism of TDDFT is used to calculate the excitation spectrum of a system. It is calculated using the Casida equation [11] as an eigenvalue problem that describes the first order response of the density. In contrast, the electron density is directly propagated in time under the real time (RT) formalism. RTTDDFT can be used to calculate the nonlinear response of the density

under strong perturbations such as ultrafast electron dynamics with strong laser fields [12].

There are multiple components that must be decided for RTTDDFT calculations. These include preparation of the initial density and orbitals, choice of the exchange-correlation functional, the form of the time-dependent potential which is determined by the problem to be solved and the choice of the time-propagation scheme. The time evolution is a significant fraction of the computational cost [13, 14].

Machine learning (ML) for accelerating scientific simulations is a rapidly growing area of research [15]. A variety of unsupervised and data-driven models have been developed to solve differential equations across a wide range of domains [16].

Neural operators (NOs) [17] are a class of models that map function-to-function spaces, as opposed to the finite-dimensional vector space mappings of neural networks. This is especially useful for partial differential equation (PDE) problems where experimental or simulation data is available. Fourier neural operators (FNOs) [18] are a type of NO which represent operator weights in Fourier space. The main advantages of FNOs are that they generalize well across function spaces, and being resolution-invariant, they can be used for inference on higher resolution grids than the training set grids. FNOs have also been used for forward and inverse PDE problems in various domains [19].

While many applications of ML have been developed for ground state DFT [20, 21, 22], there have been relatively fewer efforts focused on TDDFT. Some applications of ML for TDDFT include development of exchange-correlation potentials [23, 24] and predicting properties such as spectra and stopping power [25].

In this work, we demonstrate the effectiveness of FNOs in propagating the electron density in time under the TDDFT framework. Instead of propagating orbitals in time as done conventionally in terms of the time-dependent Kohn-Sham equations, we use the FNO propagator to directly evolve the density. This has two advantages: the computational cost does not scale with the number of orbitals and larger propagation time steps can be used, thus using fewer iterations. Section 2 contains a brief description of TDDFT, FNOs and our proposed autoregressive model. Section 3 contains results obtained with this model for the time evolution of one-dimensional diatomic molecules under the influence of an oscillating laser pulse. We show that the model can be generalized across ionic configurations, is faster and more accurate than comparable numerical simulations and can also be used for higher resolution grids. We discuss the physical viability of the predicted densities, and then offer conclusion in Section 5.

We use atomic units a.u. ($\hbar = m_e = e = 1$) unless specified otherwise.

2. Methods

2.1. Time-Dependent Density Functional Theory

The time-dependent many-body Schrödinger equation describes the dynamics of systems composed of multiple interacting particles. A common problem is interacting electrons in atoms and molecules, for which the Schrödinger equation is

$$i \frac{\partial}{\partial t} \Psi(\underline{\mathbf{r}}, t) = \hat{H}(t) \Psi(\underline{\mathbf{r}}, t), \quad (1)$$

where $\underline{\mathbf{r}}$ represents the collective coordinates of the N electrons, $\Psi(\underline{\mathbf{r}}, t)$ is the many-body wavefunction and \hat{H} is the Hamiltonian operator, representing the total energy of the system. For this problem the form of \hat{H} is $\hat{H}(t) = \hat{T} + \hat{W} + \hat{V}(t)$, where $\hat{T} = \sum_{j=1}^N -\nabla_j^2/2$ is the kinetic energy operator, $\hat{W} = \sum_{1 \leq j < k \leq N} \frac{1}{|\mathbf{r}_j - \mathbf{r}_k|}$ represents the electron-electron interaction, and $\hat{V}(t) = v_{\text{ext}}(\mathbf{r}, t)$ is the time-dependent external potential operator which includes the static external potential due to the ions and an external time-dependent potential that drives the system. Note that in writing this Schrödinger equation we are assuming the Born-Oppenheimer approximation, i.e. we are treating the dynamics of the ions as occurring on a much longer time scale than the dynamics of the electrons, and can therefore treat the ions as classical point-like particles. The initial state $\Psi(\underline{\mathbf{r}}) = \Psi(\underline{\mathbf{r}}, t_0)$ is obtained by solving the time-independent Schrödinger equation

$$\hat{H} \Psi(\underline{\mathbf{r}}) = E \Psi(\underline{\mathbf{r}}) \quad (2)$$

which is an eigenvalue problem where E denotes the eigenvalues and corresponds to the total energy of the system.

The many-body wavefunction Ψ contains all the information about the system and can be used to calculate its properties. However for 3 spatial dimensions, we need to solve a system of $3N$ variables and the computational cost scales exponentially with N , rendering it intractable for all but the simplest systems.

DFT and TDDFT allow us to solve Eq. 2 and Eq. 1 respectively by reformulating the problem in terms of electron density rather than the wavefunction, dramatically reducing the number of variables from $3N$ to 3.

The Runge-Gross theorem [1] states that for a system with a given ground state many-body wavefunction $\Psi_0 = \Psi_0(\mathbf{r}, t_0)$, there exists a unique mapping between the potential and the time-dependent density. The density can be obtained by solving a system of fictitious non-interacting particles governed by the time-dependent Kohn-Sham (TDKS) equations [26]

$$\hat{H}_{\text{KS}} \phi_j(\mathbf{r}, t) = i \frac{\partial \phi_j(\mathbf{r}, t)}{\partial t}, \quad j = 1, \dots, N, \quad (3)$$

where the electron density

$$n(\mathbf{r}, t) = \sum_{j=1}^N |\phi_j(\mathbf{r}, t)|^2 \quad (4)$$

is the quantity of interest. The Kohn-Sham Hamiltonian is defined as

$$\hat{H}_{\text{KS}} = -\frac{1}{2}\nabla^2 + v_s[n](\mathbf{r}, t), \quad (5)$$

where the Kohn-Sham potential $v_s[n](\mathbf{r}, t)$ is a functional of the density $n(\mathbf{r}, t)$. The correspondence between density and potential is established through

$$v_s[n](\mathbf{r}, t) = v_{\text{ext}}(\mathbf{r}, t) + v_{\text{H}}[n](\mathbf{r}, t) + v_{\text{xc}}[n](\mathbf{r}, t), \quad (6)$$

with $v_{\text{ext}}(\mathbf{r}, t)$ the external potential, $v_{\text{H}}(\mathbf{r}, t)$ the Hartree potential, and $v_{\text{xc}}(\mathbf{r}, t)$ the exchange-correlation potential. The external potential is composed of the ionic potential and any time-dependent external perturbation such as a laser field.

While in theory, $v_{\text{xc}}(\mathbf{r}, t)$ depends on the density at all previous time steps, the adiabatic approximation is often used in practice [27]. We use the adiabatic local density approximation (ALDA). Under ALDA, $v_{\text{xc}}(\mathbf{r}, t)$ is approximated as:

$$v_{\text{xc}}^{\text{ALDA}}[n, \Psi_0, \Phi_0](\mathbf{r}, t) = v_{\text{xc}}^{\text{LDA}}[n](\mathbf{r}, t), \quad (7)$$

where $v_{\text{xc}}^{\text{LDA}}$ is the LDA exchange-correlation potential in ground-state DFT.

These coupled equations are solved through iterative numerical algorithms which represent a significant computational cost in the TDDFT workflow [13].

2.1.1. Time Propagators The general form of the time evolution operator \hat{U} for a time domain T is given by:

$$\phi_i(\mathbf{r}, T) = \hat{U}(T, 0)\phi_i(\mathbf{r}, 0). \quad (8)$$

When the Hamiltonian \hat{H}_{KS} is time-independent, $\hat{U}(T, t_0) = \exp(-i\hat{H}_{\text{KS}}(T - t_0))$. However, in the general case, when external fields are present or due to the inherent time-dependence of the density within the Hamiltonian functional, $\hat{H}_{\text{KS}}(t)$ is time-dependent. The solution then requires a time-ordered exponential:

$$\hat{U}(T, t_0) = \mathcal{T} \exp \left(-i \int_{t_0}^T \hat{H}_{\text{KS}}(t') dt' \right), \quad (9)$$

where \mathcal{T} is the time-ordering operator.

Evaluating the time-ordered exponential directly is generally intractable. In practice, the total time evolution is broken down into a sequence of short time steps Δt . The total evolution operator over a time domain T starting from $t_0 = 0$ is approximated as a product of short-time propagators:

$$\hat{U}(T, 0) = \prod_{j=0}^{N-1} \hat{U}(t_{j+1}, t_j), \quad (10)$$

with $t_0 = 0$, $t_{j+1} = t_j + \Delta t_j$, and $t_N = T$. Usually, a constant time step Δt is used. The accuracy and stability of the simulation depend crucially on the approximation used for the short-time propagator $\hat{U}(t_j + \Delta t, t_j)$.

A fundamental requirement for the exact evolution operator is unitarity: $\hat{U}^\dagger(t + \Delta t, t) = \hat{U}^{-1}(t + \Delta t, t)$. This property ensures that the norm of the wavefunctions is

conserved over time, $\langle \phi_i(t) | \phi_i(t) \rangle = \text{const}$, which in turn guarantees the conservation of the total number of electrons (i.e., the integrated density $\int n(\mathbf{r}, t) d\mathbf{r}$). Another important property is time-reversal symmetry: $\hat{U}(t + \Delta t, t) = \hat{U}^{-1}(t, t + \Delta t)$, meaning that propagating forward by Δt is the inverse of propagating backward by Δt . A robust numerical time propagation algorithm should ideally preserve these properties, or approximate them sufficiently well to ensure physical conservation laws and stability over the desired simulation time.

Numerous methods have been developed and analyzed for approximating the short-time propagator $\hat{U}(t_j + \Delta t, t_j)$ [13, 14]. Common approaches include:

- Magnus expansions, which attempt to approximate the exponent in $\hat{U}(\Delta t) = \exp(\hat{\Omega}(\Delta t))$.
- Split-operator methods, particularly useful when the Hamiltonian can be split into analytically solvable parts (e.g., kinetic and potential terms).
- Runge-Kutta methods (explicit and implicit), adapted for the Schrödinger equation.
- Exponential midpoint and other exponential integrators.
- Implicit methods like the Crank-Nicolson scheme [28].

The choice of propagator often involves a trade-off between accuracy, stability (especially concerning the maximum usable time step Δt), computational cost per step, and conservation properties.

For this work, the reference data for training our neural network model was generated using the Crank-Nicolson method [28]. This is an implicit method, formulated as:

$$\begin{aligned} \left(1 + \frac{i\Delta t}{2} \hat{H}_{KS}(t + \Delta t/2)\right) \phi_i(t + \Delta t) \approx \\ \left(1 - \frac{i\Delta t}{2} \hat{H}_{KS}(t + \Delta t/2)\right) \phi_i(t) \end{aligned} \quad (11)$$

where $\hat{H}_{KS}(t + \Delta t/2)$ is typically an approximation of the Hamiltonian at the midpoint of the time step. The Crank-Nicolson propagator, $\hat{U}_{CN}(\Delta t) \approx [1 + i\hat{H}_{KS}\Delta t/2]^{-1}[1 - i\hat{H}_{KS}\Delta t/2]$, is unitary and stable, although its implicit nature requires solving a linear system at each time step.

While these traditional methods propagate the Kohn-Sham orbitals ϕ_i , our approach deviates from this standard procedure. We train a Fourier Neural Operator (FNO) to directly propagate the electron density $n(\mathbf{r}, t)$ in time with larger Δt , bypassing the explicit evolution of the single-particle orbitals.

2.1.2. Model Systems We consider an external potential

$$v_{\text{ext}}(\mathbf{r}, t) = v_{\text{ion}}(\mathbf{r}) + v_{\text{las}}(t), \quad (12)$$

where we simulate a class of one-dimensional diatomic molecules that serves as a model system with two interacting electrons under the static ionic potential:

$$v_{\text{ion}}(\mathbf{r}) = v_{\text{ion}}(x) = -\frac{Z_1}{\sqrt{(x - \frac{d}{2})^2 + a^2}} - \frac{Z_2}{\sqrt{(x + \frac{d}{2})^2 + a^2}}, \quad (13)$$

where Z_1 and Z_2 denote the charge of the atoms, d denotes the bond length, and a is a softening parameter for numerical stability.

The system is excited with a laser given by a time-dependent external potential:

$$v_{\text{las}}(t) = A \sin \omega t. \quad (14)$$

Here we assume the dipole approximation, where we can treat the laser as spatially constant because the size of our molecule is much small than the wavelength of the laser. Given the ground state prepared with $v_{\text{ion}}(x)$, we propagate the density under the influence of the laser $v_{\text{las}}(t)$.

The domain is defined by $[-L, L]$ for time $[0, T]$ with discretization Δx and Δt . We use fixed boundary conditions

$$\phi_i(-L, t) = \phi_i(L, t) = 0, \quad \forall t \in [0, T]. \quad (15)$$

We use the LDA functional due to its simplicity and accuracy for such simple one-dimensional systems. The density evolution is calculated by solving the time-dependent Kohn-Sham equations with the external potential $v_{\text{ext}}(r, t)$ using the Crank-Nicholson scheme. The numerical simulation is performed using the Octopus RT-TDDFT code [29].

2.2. Physics-Informed Machine Learning

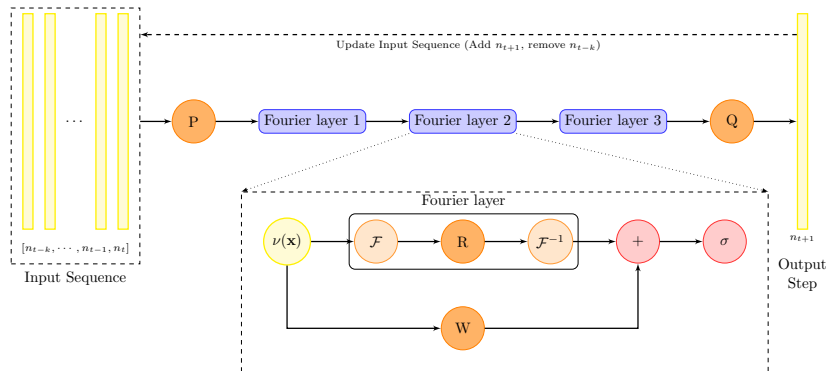


Figure 1: Autoregressive FNO architecture for predicting the density at time $t+1$ based on k previous time steps.

Neural operators (NOs) [30, 31] extend neural networks by mapping functions to functions instead of finite-dimensional vectors. While a neural network maps \mathbb{R}^n to \mathbb{R}^m , a neural operator maps function spaces, $\mathcal{G} : \mathcal{A} \rightarrow \mathcal{U}$. Our goal is to approximate the non-linear map $\mathcal{G}^\dagger : \mathcal{A} \rightarrow \mathcal{U}$ with a neural operator \mathcal{G}_θ , parameterized by $\theta \in \mathbb{R}^p$.

Training involves observations $\{(a_i, u_i)\}_{i=1}^N$ where $u_i = \mathcal{G}^\dagger(a_i)$. The objective is to find parameters θ^* minimizing the loss:

$$\theta^* = \min_{\theta \in \mathbb{R}^p} \frac{1}{N} \sum_{i=1}^N \|u_i - \mathcal{G}_\theta(a_i)\|_{\mathcal{U}}^2. \quad (16)$$

A neural operator $\mathcal{G}_\theta(a)$ is defined by the composition of layers:

$$\mathcal{G}_\theta(a) = Q \circ v_L \circ v_{L-1} \circ \dots \circ v_1 \circ P(a), \quad (17)$$

where P maps the input function a to a higher dimensional representation $v_0(x)$, Q maps the final layer's output $v_L(x)$ back to the target function space \mathcal{U} , and each intermediate layer v_{l+1} updates the representation v_l via:

$$v_{l+1}(x) = \sigma(W_l v_l(x) + (\mathcal{K}_l(a; \phi_l) v_l)(x)), \quad \forall x \in D. \quad (18)$$

Here, W_l is a learnable weights matrix which corresponds to a linear transformation, σ is a non-linear activation function applied point-wise, and \mathcal{K}_l is a non-local kernel integral operator parameterized by ϕ_l :

$$(\mathcal{K}_l(a; \phi_l) v_l)(x) = \int_D \kappa_l(x, y, a(x), a(y); \phi_l) v_l(y) dy. \quad (19)$$

The kernel function κ_l integrates information across the domain D . The parameters θ consist of the parameters of P , Q , and all W_l and ϕ_l .

The Fourier Neural Operator (FNO) [18] proposes an efficient implementation of the kernel integral operator \mathcal{K}_l . The FNO restricts the kernel integration to be a convolution operator, assuming the kernel depends only on the displacement, i.e., $\kappa_l(x, y; \phi_l) = \kappa_l(x - y; \phi_l)$. This allows the use of the Convolution Theorem, which states that a convolution in the spatial domain is equivalent to point-wise multiplication in the Fourier domain:

$$(\mathcal{K}_l v_l)(x) = (\kappa_l * v_l)(x) = \mathcal{F}^{-1}(\mathcal{F}(\kappa_l) \cdot \mathcal{F}(v_l))(x), \quad (20)$$

where \mathcal{F} denotes the Fourier transform and \mathcal{F}^{-1} its inverse. The operator \cdot represents point-wise multiplication in the Fourier domain.

Instead of learning the kernel κ_l directly in the spatial domain, the FNO parameterizes the operator directly in the Fourier domain. The Fourier coefficients $\mathcal{F}(\kappa_l)$ are represented by a complex-valued tensor R_{ϕ_l} which constitutes the learnable parameters ϕ_l for the kernel operator at layer l . The FNO truncates the Fourier series, considering only a finite number of lower-frequency modes, $k \in \{k \mid \|k\| \leq k_{\max, l}\}$, where $k_{\max, l}$ is the maximum frequency mode for layer l . This significantly reduces the number of parameters. The operation in Equation 20 is thus implemented as:

- (i) Compute the Fourier transform of the input $v_l(x)$, yielding $\mathcal{F}(v_l)(k)$.
- (ii) For each Fourier mode k up to $k_{\max, l}$, perform a linear transformation (element-wise multiplication) with the corresponding parameters in R_{ϕ_l} : $(\hat{v}_l)_k = (R_{\phi_l})_k \cdot (\mathcal{F}(v_l))_k$.
- (iii) Compute the inverse Fourier transform of the result: $\mathcal{F}^{-1}(\hat{v}_l)(x)$.

The update rule for the FNO layer becomes:

$$v_{l+1}(x) = \sigma \left(W_l v_l(x) + \mathcal{F}^{-1} (R_{\phi_l} \cdot (\mathcal{F}(v_l))) (x) \right). \quad (21)$$

This formulation has several advantages. The Fast Fourier Transform (FFT) algorithm allows computing \mathcal{F} and \mathcal{F}^{-1} efficiently, typically in $\mathcal{O}(n \log n)$ time, where n is the number of discretization points. The parameterization in the Fourier domain makes the FNO discretization-invariant, meaning the same learned operator can be evaluated on different mesh resolutions without retraining. The number of modes k_{\max} and the width of the channel dimensions (determined by Q, P and W_l) control the expressivity and complexity of the model. By stacking these layers, FNOs can effectively capture complex, non-linear dependencies between functions while maintaining computational efficiency.

2.3. Time-Propagator Design

To model the evolution of the electron density $n(x, t)$ under the influence of a time-dependent external potential $v_l(t)$, we employ an autoregressive approach based on the Fourier Neural Operator (FNO). The FNO architecture is well-suited for learning resolution-invariant mappings between infinite-dimensional function spaces, making it appropriate for processing spatio-temporal data like the electron density [?]. The autoregressive framework allows the model to predict future states based on a sequence of past observations and the corresponding external potential values.

Let \mathbf{n}_t represent the discretized electron density on a spatial grid at time step t , and let $v_{l,t}$ be the value of the external potential at the same time step t . The model takes as input a sequence of the past T_{in} density grids and the corresponding potential values to predict the density grid at the next time step, $t + 1$.

The input density sequence at time step t is denoted by:

$$\mathbf{N}_t = [\mathbf{n}_{t-T_{\text{in}}+1}, \mathbf{n}_{t-T_{\text{in}}+2}, \dots, \mathbf{n}_t], \quad (22)$$

and the corresponding input potential sequence is:

$$\mathbf{V}_{l,t} = [v_{l,t-T_{\text{in}}+1}, v_{l,t-T_{\text{in}}+2}, \dots, v_{l,t}]. \quad (23)$$

The initial input sequences, \mathbf{N}_0 and $\mathbf{V}_{l,0}$, consist of the first T_{in} time steps, starting with the ground state density \mathbf{n}_0 and the initial potential values.

The FNO model, denoted by \mathcal{G}_θ with trainable parameters θ , maps the input sequences to the predicted density at the next time step, $\hat{\mathbf{n}}_{t+1}$:

$$\hat{\mathbf{n}}_{t+1} = \mathcal{G}_\theta(\mathbf{N}_t, \mathbf{V}_{l,t}). \quad (24)$$

Here, the model implicitly learns time propagation through the recent history of the density, the applied potential, and the subsequent density state.

Following the prediction of $\hat{\mathbf{n}}_{t+1}$, the input sequences are updated for the next prediction step ($t + 1 \rightarrow t + 2$). The new density sequence \mathbf{N}_{t+1} is formed by appending the predicted density $\hat{\mathbf{n}}_{t+1}$ and removing the oldest density grid $\mathbf{n}_{t-T_{\text{in}}+1}$:

$$\mathbf{N}_{t+1} = [\mathbf{n}_{t-T_{\text{in}}+2}, \mathbf{n}_{t-T_{\text{in}}+3}, \dots, \mathbf{n}_t, \hat{\mathbf{n}}_{t+1}]. \quad (25)$$

Similarly, the potential sequence is updated by incorporating the next known potential value $v_{l,t+1}$ and removing the oldest value:

$$\mathbf{V}_{l,t+1} = [v_{l,t-T_{\text{in}}+2}, v_{l,t-T_{\text{in}}+3}, \dots, v_{l,t}, v_{l,t+1}]. \quad (26)$$

This autoregressive process, illustrated in Figure 1, is repeated iteratively to generate the density evolution over the desired time period.

2.3.1. Input Representation Design The autoregressive FNO framework requires an effective representation of both the electron density history and the time-dependent external potential. We implement multiple input representation strategies to capture the complex spatio-temporal dependencies between these quantities.

Let $\mathbf{n}_t \in \mathbb{R}^{n_x}$ denote the discretized electron density on a spatial grid of size n_x at time t , and let $v_{l,t} \in \mathbb{R}$ be the external potential value. The input representation module P maps these inputs to a higher-dimensional feature space suitable for the FNO layers.

We define the density input sequence as:

$$\mathbf{N}_t = [\mathbf{n}_{t-T_{\text{in}}+1}, \dots, \mathbf{n}_t] \in \mathbb{R}^{n_x \times T_{\text{in}}}, \quad (27)$$

and the potential sequence as:

$$\mathbf{V}_{l,t} = [v_{l,t-T_{\text{in,laser}}+1}, \dots, v_{l,t}] \in \mathbb{R}^{n_x \times T_{\text{in,laser}}}, \quad (28)$$

where T_{in} and $T_{\text{in,laser}}$ denote the number of past time steps for density and potential inputs, respectively. Additionally, we optionally include the spatial grid coordinates $\mathbf{g} \in \mathbb{R}^{n_x \times 1}$.

We implement five distinct input representation strategies:

1. Density-Only Representation: This baseline approach uses only the density history:

$$P_{\text{density}}(\mathbf{N}_t, \mathbf{g}) = W_d[\mathbf{N}_t, \mathbf{g}], \quad (29)$$

where $W_d \in \mathbb{R}^{w \times (T_{\text{in}}+1)}$ maps to the model width w , and $[\cdot, \cdot]$ denotes concatenation along the feature dimension.

2. Direct Concatenation: A straightforward approach that concatenates all inputs:

$$P_{\text{concat}}(\mathbf{N}_t, \mathbf{V}_{l,t}, \mathbf{g}) = W_c[\mathbf{N}_t, \mathbf{V}_{l,t}, \mathbf{g}], \quad (30)$$

where $W_c \in \mathbb{R}^{w \times (T_{\text{in}}+T_{\text{in,laser}}+1)}$.

3. Separate Processing with Concatenation: This approach processes density and potential through independent transformations before concatenation:

$$P_{\text{sep-concat}}(\mathbf{N}_t, \mathbf{V}_{l,t}, \mathbf{g}) = [W_d[\mathbf{N}_t, \mathbf{g}], W_l \mathbf{V}_{l,t}], \quad (31)$$

where $W_d \in \mathbb{R}^{w \times (T_{\text{in}}+1)}$ and $W_l \in \mathbb{R}^{w \times T_{\text{in,laser}}}$, yielding an output dimension of $2w$.

4. Separate Processing with Addition: The default representation processes inputs independently and combines them additively:

$$P_{\text{sep-add}}(\mathbf{N}_t, \mathbf{V}_{l,t}, \mathbf{g}) = W_d[\mathbf{N}_t, \mathbf{g}] + W_l \mathbf{V}_{l,t}, \quad (32)$$

maintaining the output dimension w .

5. Space-Time Convolution: This approach treats the input as a 2D spatio-temporal field. The density and potential sequences are reshaped and stacked:

$$\mathbf{X} = \begin{bmatrix} \mathbf{N}_t^T \\ \mathbf{V}_{l,t}^T \end{bmatrix} \in \mathbb{R}^{2 \times T_{\text{in}} \times n_x}. \quad (33)$$

where we pad $\mathbf{V}_{l,t}$ to match T_{in} if necessary. A 2D convolutional operator with kernel $\mathcal{K}_{\text{st}} \in \mathbb{R}^{w \times 2 \times k_t \times k_x}$ is applied:

$$P_{\text{st-conv}}(\mathbf{N}_t, \mathbf{V}_{l,t}, \mathbf{g}) = \text{AvgPool}_t(\mathcal{K}_{\text{st}} * \mathbf{X}) + W_g \mathbf{g}, \quad (34)$$

where $*$ denotes 2D convolution, AvgPool_t performs temporal averaging, and $W_g \in \mathbb{R}^{w \times 1}$ incorporates spatial grid information.

The choice of input representation affects the model's ability to capture different types of dependencies. The separate processing approaches (3 and 4) allow the model to learn distinct features for density and potential before combination, while the space-time convolution explicitly models spatio-temporal correlations through convolutional filters. The output of the input representation module P serves as the initial feature representation $v_0(x)$ for the subsequent FNO layers.

2.3.2. Observable Calculations To evaluate the physical validity and accuracy of the predicted electron densities, we compute several key observables from both the predicted and reference density fields.

Integrated Density (Particle Number): The total number of electrons is computed by integrating the density over the spatial domain:

$$N(t) = \int_{-\infty}^{\infty} n(x, t) dx \approx \sum_{i=1}^{n_x} n(x_i, t) \Delta x, \quad (35)$$

where n_x is the number of spatial grid points and Δx is the grid spacing. For our systems, this integral should remain constant at $N = 2$ throughout the evolution, serving as a fundamental conservation check.

Dipole Moment: The dipole moment characterizes the charge distribution asymmetry and is particularly sensitive to the system's response to the external field:

$$\mu(t) = \int_{-\infty}^{\infty} x n(x, t) dx \approx \sum_{i=1}^{n_x} x_i n(x_i, t) \Delta x. \quad (36)$$

The time-dependent dipole moment directly relates to the optical response and provides insight into the collective electron dynamics.

Total Energy: Within the Thomas-Fermi approximation, the total energy functional consists of kinetic, Hartree, and external potential contributions. The kinetic energy is approximated as:

$$E_K[n] = \frac{\pi^2}{6} \int_{-\infty}^{\infty} n(x, t)^3 dx \approx \frac{\pi^2}{6} \sum_{i=1}^{n_x} n(x_i, t)^3 \Delta x. \quad (37)$$

The Hartree energy accounts for electron-electron repulsion:

$$E_H[n] = \frac{1}{2} \int_{-\infty}^{\infty} \int_{-\infty}^{\infty} \frac{n(x, t)n(x', t)}{|x - x'|} dx dx', \quad (38)$$

which we evaluate numerically using a soft-Coulomb regularization:

$$E_H[n] \approx \frac{1}{2} \sum_{i,j=1}^{n_x} \frac{n(x_i, t)n(x_j, t)}{\sqrt{(x_i - x_j)^2 + a^2}} (\Delta x)^2, \quad (39)$$

where a is a small regularization parameter.

The external potential energy includes contributions from both the ionic potential $v_{\text{ion}}(x)$ and the time-dependent laser field $v_l(t)$:

$$E_{\text{ext}}[n] = \int_{-\infty}^{\infty} n(x, t)[v_{\text{ion}}(x) + v_l(t)] dx. \quad (40)$$

The total energy is then:

$$E_{\text{tot}}[n] = E_K[n] + E_H[n] + E_{\text{ext}}[n]. \quad (41)$$

These observables are computed at each time step for both predicted and reference densities. The absolute errors in these quantities provide quantitative measures of the model's physical accuracy beyond point-wise density comparisons. The dipole moment error is particularly important as it directly relates to effects of the time-dependent laser field, while energy conservation provides a test of the model's ability to capture the system's dynamics correctly.

2.3.3. Physics-Informed Loss Functions To enhance the physical consistency of the predictions, we incorporate physics-informed loss terms alongside the standard data-driven loss. The combined loss function takes the form:

$$\mathcal{L}_{\text{total}} = \mathcal{L}_{\text{data}} + \lambda_1 \mathcal{L}_{\text{int}} \quad (42)$$

where λ_1 is a hyperparameter that control the relative importance of each the integral constraint.

Data-Driven Loss: The primary loss term measures the point-wise discrepancy between predicted and reference densities:

$$\mathcal{L}_{\text{data}} = \frac{1}{|\mathcal{D}|} \sum_{d \in \mathcal{D}} \frac{1}{|\mathcal{T}|} \sum_{t \in \mathcal{T}} \left\| \mathbf{n}_t^{(d)} - \hat{\mathbf{n}}_t^{(d)} \right\|_2^2, \quad (43)$$

where \mathcal{D} denotes the training dataset and \mathcal{T} the set of predicted time steps.

Integral Conservation Loss: This term enforces particle number conservation:

$$\mathcal{L}_{\text{int}} = \frac{1}{|\mathcal{D}|} \sum_{d \in \mathcal{D}} \frac{1}{|\mathcal{T}|} \sum_{t \in \mathcal{T}} \left(\sum_i \hat{n}_{t,i}^{(d)} \Delta x - N_{\text{ref}}^{(d)} \right)^2, \quad (44)$$

where $N_{\text{ref}}^{(d)} = 2$ is the reference number of electrons for system d .

The inclusion of physics-informed losses not only improves the physical plausibility of the predictions but also enhances the model's generalization to systems outside the training distribution.

2.3.4. Error Metrics To evaluate model performance, we employ multiple error metrics that capture different aspects of prediction accuracy for both point-wise density fields and integrated observables.

Mean Squared Error (MSE): The MSE quantifies the average squared deviation between predicted and reference values:

$$\text{MSE} = \frac{1}{n} \sum_{i=1}^n (y_i - \hat{y}_i)^2, \quad (45)$$

where y_i and \hat{y}_i denote reference and predicted values, respectively. For density fields, this is computed point-wise across all spatial locations and time steps.

Mean Absolute Error (MAE): The MAE provides a more interpretable measure of average prediction error:

$$\text{MAE} = \frac{1}{n} \sum_{i=1}^n |y_i - \hat{y}_i|. \quad (46)$$

Unlike MSE, MAE is less sensitive to outliers and provides errors in the same units as the predicted quantity.

Mean Absolute Percentage Error (MAPE): For observables with varying magnitudes, MAPE normalizes the error relative to the reference value:

$$\text{MAPE} = \frac{100}{n} \sum_{i=1}^n \left| \frac{y_i - \hat{y}_i}{y_i} \right|, \quad (47)$$

where we apply a small tolerance $\epsilon = 10^{-6}$ to avoid division by zero: $\max(|y_i|, \epsilon)$.

Symmetric Mean Absolute Percentage Error (SMAPE): To address the asymmetry in MAPE, we also compute:

$$\text{SMAPE} = \frac{100}{n} \sum_{i=1}^n \frac{|y_i - \hat{y}_i|}{(|y_i| + |\hat{y}_i|)/2 + \epsilon}. \quad (48)$$

SMAPE provides a bounded percentage error that treats over- and under-predictions symmetrically.

For density fields, we primarily report MSE and MAE computed point-wise across the spatial grid and averaged over time. For observables, particularly the dipole moment where values can approach zero, we employ all four metrics to provide a comprehensive assessment. The percentage-based metrics (MAPE and SMAPE) are especially valuable for the dipole moment, as its magnitude varies significantly during the laser pulse interaction, making absolute errors less informative. Visualizations, like those shown in Figure 2, comparing the predicted and reference density evolution provide qualitative assessment.

3. Results

3.1. Dataset and Computational Setup

We evaluate our autoregressive FNO model on a comprehensive dataset of time-dependent density functional theory (TDDFT) simulations. The dataset comprises

2048 independent simulations of diatomic systems with varying nuclear charges (Z_1, Z_2), internuclear distances d , and laser field parameters including intensity and wavelength. Each simulation is performed on a spatial grid of 361 points with spacing $\Delta x = 0.05$ a.u., covering the domain $[-9.0, 9.0]$ a.u. The temporal evolution spans $[0.0, 10.0]$ fs with 51 time steps at $\Delta t = 0.1$ fs resolution.

The reference data is generated using the Octopus real-space TDDFT code with a fine temporal resolution of $\Delta t = 0.01$ fs to ensure numerical accuracy. For consistent comparison with our model predictions, we also compute reference solutions at the coarser $\Delta t = 0.1$ fs resolution using the same TDDFT solver. This allows us to demonstrate the accuracy of the model with larger time steps. We filter the dataset to remove systems with low time-dependent variation and systems with numerical artifacts such as boundary reflections. The final dataset consists of 800 training systems, 150 validation systems and 200 test systems representing various input conditions and laser parameters.

3.2. Baseline Performance and Ablation Studies

We first establish baseline performance by comparing different input representation strategies and conducting ablation studies on key architectural components. Table 1 summarizes the performance metrics across model configurations with different input encodings on the test set.

Table 1: Comparison of error metrics across input representations.

Metric	Density Only	Concat	FC Add	FC Concat	Spacetime Conv
AE (10^{-3})	1.97	0.899	0.872	0.879	1.48
MSE (10^{-5})	6.15	3.13	3.20	3.27	5.08
MAPE (%)	3.71	1.90	1.84	1.85	3.80
Dipole MSE (10^{-3})	11.4	6.75	7.37	7.27	8.92
Dipole MAPE (%)	27.6	18.6	9.35	10.7	27.0
Integral (≈ 2)	1.9990	2.0000	1.9995	2.0000	2.0005
Inference Time (ms)	1.33	1.32	1.35	1.38	1.51

The results demonstrate that incorporating laser information significantly improves prediction accuracy compared to the density-only baseline. The accuracy of the FNO model with Octopus numerical calculations on the same time grid can be compared in Table 2. The FNO model achieves much better adherence to the simulations generated on a higher resolution grid, at a much lower inference cost on the coarse grid.

3.3. Generalization Capabilities

To assess the model’s ability to generalize beyond the training distribution, we evaluate its performance on two challenging scenarios: spatial super-resolution and extended

Table 2: Comparison of error metrics across models.

Metric	Baseline FNO	Octopus Coarse	Temporal Extension
AE (10^{-3})	0.872	6.10	0.910
MSE (10^{-5})	3.20	31.2	2.56
MAPE (%)	1.84	853	2.63
SMAPE (%)	1.73	62.3	2.15
Dipole MSE (10^{-3})	7.37	79.0	5.54
Dipole MAPE (%)	9.35	74.0	10.8
Dipole SMAPE (%)	6.08	51.1	6.76
Integral (≈ 2)	1.9995 ± 0.0014	$2.0000 \pm 2.0\text{e-}7$	$1.9995 \pm 9.7\text{e-}4$
Inference Time (ms)	1.35 ± 0.03	—	3.10 ± 5.5

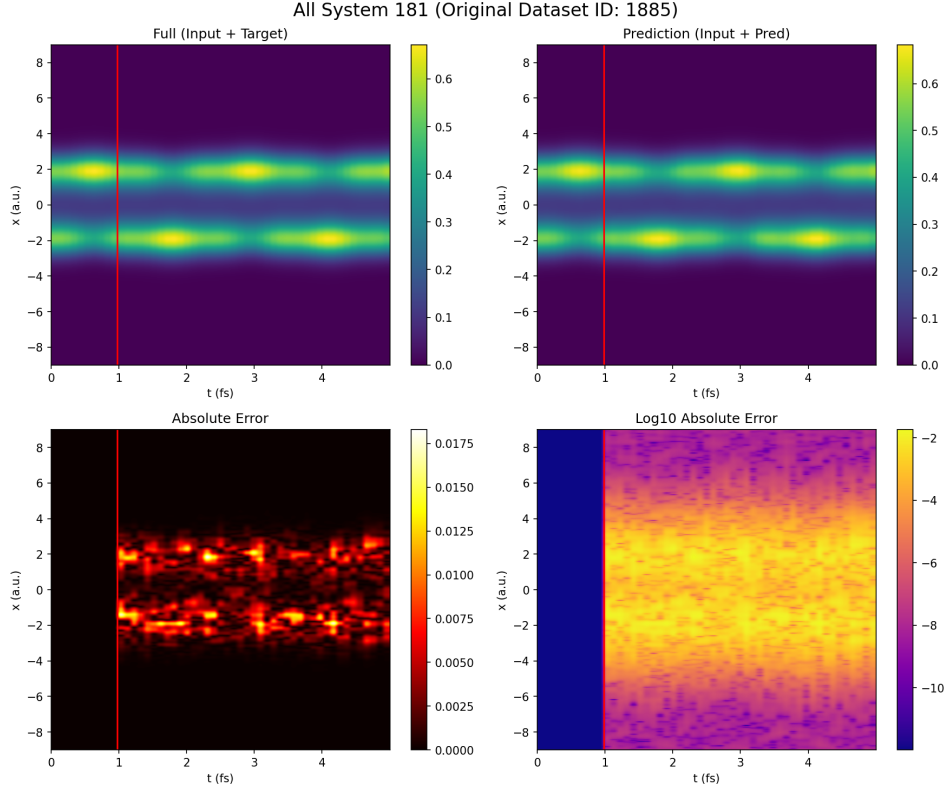


Figure 2: Results for a representative system.

temporal rollout.

Spatial Super-resolution: We test the trained model on systems discretized with twice the spatial resolution ($\Delta x = 0.025$ a.u., 721 grid points). The FNO’s spectral representation enables direct evaluation at the higher resolution without retraining.

Extended Temporal Rollout: While the model is trained on sequences up to 5.0 fs, we evaluate its long-term prediction stability by extending the autoregressive rollout

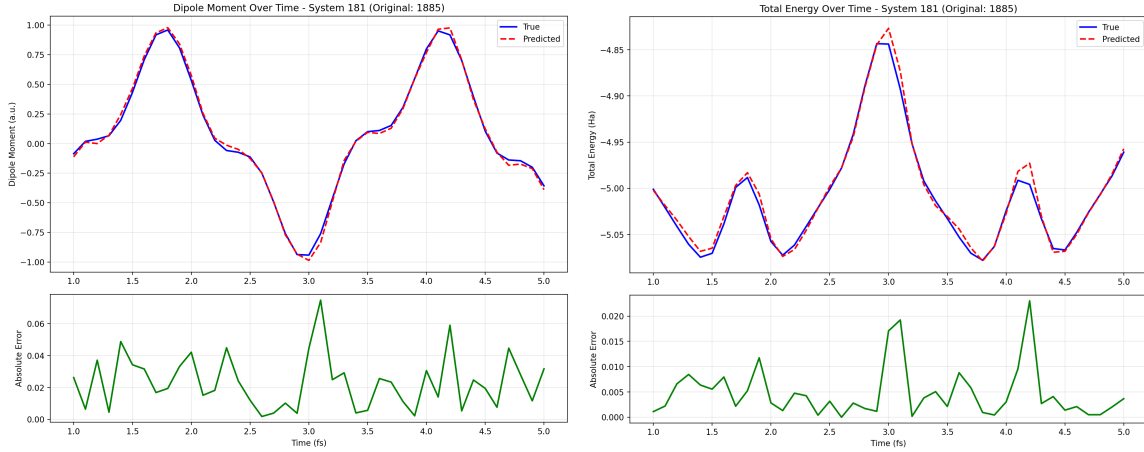


Figure 3: Observables calculated for the representative system.

Left: Dipole moment calculated from reference and predicted density. Right: Total TF energy calculated from reference and predicted density.

to 10.0 fs. The model exhibits stable propagation without accumulating catastrophic errors. As shown in Table 2, the error metrics for [0-10.0] fs time domain evolution are consistent with the baseline model trained only on [0-5.0] fs time domain.

3.4. Observable Predictions

Beyond point-wise density accuracy, we evaluate the model’s ability to predict physically meaningful observables that are critical for understanding the system’s dynamics.

Dipole Moment: Figure 3 compares predicted and reference dipole moments for representative systems. The model accurately captures the oscillatory behavior during laser excitation without error accumulation.

Total Energy: Within the Thomas-Fermi approximation, we compute the total energy functional comprising kinetic, Hartree, and external potential contributions. Figure 3 shows the temporal evolution of predicted versus reference total energies.

3.5. Time-Propagator Properties

We investigate whether the learned time-propagator exhibits fundamental physical properties expected from the underlying quantum dynamics.

Density Conservation: A fundamental requirement for any valid time evolution is the conservation of total particle number. Figure 4 shows the integrated density $N(t) = \int n(x,t)dx$ over time for model predictions. The inclusion of the integral conservation loss term \mathcal{L}_{int} ensures that particle number remains within 0.1% of the reference value throughout the evolution. This constraint is important for preventing unphysical density accumulation or depletion that can arise in purely data-driven approaches.

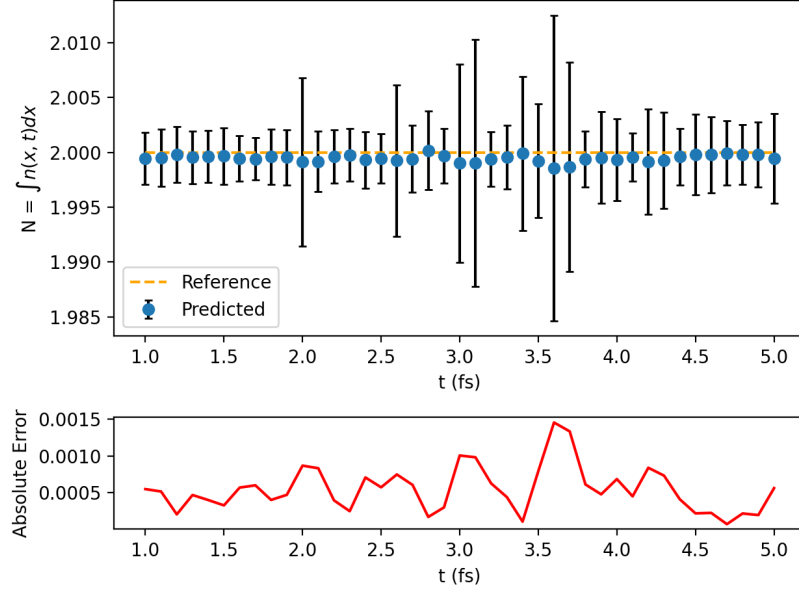


Figure 4: Evolution of predicted density norm vs. time, across all systems

Time Reversal: To test whether the model has learned a physically consistent time-evolution operator, we examine its behavior under time reversal. Starting from a state at $t = 5.0$ fs, we apply the model with reversed laser fields to propagate backward to $t = 0$. Figure 5 shows the time-reversal prediction metrics for a representative system.

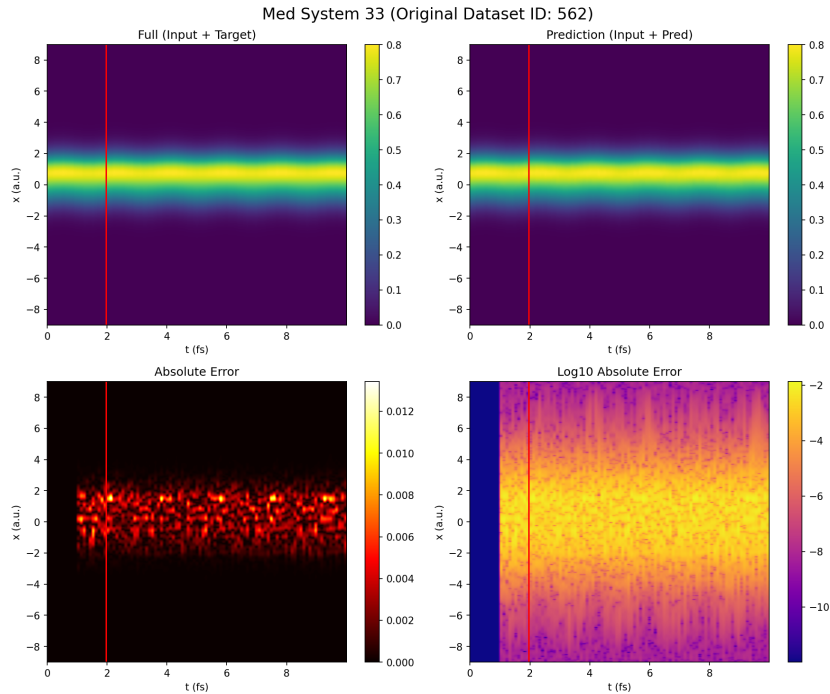


Figure 5: Representative system calculated in reverse-time order.

4. Conclusion

We show that machine learned time propagators have the potential to accelerate TDDFT calculations. The propagator generalizes well to longer time roll-out periods and higher resolution spatial grids while maintaining physical consistency and observable accuracy. Extending this work to physics-informed three-dimensional models would enable on-the-fly modeling of the electronic response properties of laser-excited molecules and materials in various scattering experiments that are conducted at photon sources around the globe. This would enable fast simulations that generalize well over the input parameters of the experimental setup. Rapid modeling would also enable the design of laser pulses to precisely control quantum dynamics under quantum optimal control theory [32].

Acknowledgments

This work was supported by the Center for Advanced Systems Understanding (CASUS), which is financed by Germany’s Federal Ministry of Education and Research (BMBF) and by the Saxon state government out of the State budget approved by the Saxon State Parliament. We acknowledge funding from the Helmholtz Association’s Initiative and Networking Fund through Helmholtz AI.

- [1] Erich Runge and E. K. U. Gross. Density-Functional Theory for Time-Dependent Systems. *Physical Review Letters*, 52(12):997–1000, March 1984. Publisher: American Physical Society.
- [2] Carlo Adamo and Denis Jacquemin. The calculations of excited-state properties with Time-Dependent Density Functional Theory. *Chemical Society Reviews*, 42(3):845–856, January 2013. Publisher: The Royal Society of Chemistry.
- [3] Neepa T. Maitra. Charge transfer in time-dependent density functional theory. *Journal of Physics: Condensed Matter*, 29(42):423001, September 2017. Publisher: IOP Publishing.
- [4] Dillon C. Yost, Yi Yao, and Yosuke Kanai. Examining real-time time-dependent density functional theory nonequilibrium simulations for the calculation of electronic stopping power. *Physical Review B*, 96(11):115134, September 2017. Publisher: American Physical Society.
- [5] Denis Jacquemin, Benedetta Mennucci, and Carlo Adamo. Excited-state calculations with TD-DFT: from benchmarks to simulations in complex environments. *Physical Chemistry Chemical Physics*, 13(38):16987–16998, 2011. Publisher: Royal Society of Chemistry.
- [6] Vladimir Goncharov. *Non-Linear Optical Response in Atoms, Molecules and Clusters: An Explicit Time Dependent Density Functional Approach*. Springer, September 2014.
- [7] Connor J. Herring and Matthew M. Montemore. Recent Advances in Real-Time Time-Dependent Density Functional Theory Simulations of Plasmonic Nanostructures and Plasmonic Photocatalysis. *ACS Nanoscience Au*, 3(4):269–279, August 2023.
- [8] Daniele Varsano, Rosa Di Felice, Miguel A. L. Marques, and Angel Rubio. A TDDFT Study of the Excited States of DNA Bases and Their Assemblies. *The Journal of Physical Chemistry B*, 110(14):7129–7138, April 2006.
- [9] Ravithree D. Senanayake, David B. Lingerfelt, Gowri U. Kuda-Singappulige, Xiaosong Li, and Christine M. Aikens. Real-Time TDDFT Investigation of Optical Absorption in Gold Nanowires. *The Journal of Physical Chemistry C*, 123(23):14734–14745, June 2019.
- [10] Ofer Neufeld, Nicolas Tancogne-Dejean, and Angel Rubio. Benchmarking Functionals for Strong-Field Light-Matter Interactions in Adiabatic Time-Dependent Density Functional Theory. *The Journal of Physical Chemistry Letters*, 15(28):7254–7264, July 2024.
- [11] Mark E. Casida. Time-Dependent Density Functional Response Theory for Molecules. In

- Recent Advances in Computational Chemistry*, volume 1, pages 155–192. WORLD SCIENTIFIC, November 1995.
- [12] Makenzie R. Provorse and Christine M. Isborn. Electron dynamics with real-time time-dependent density functional theory. *International Journal of Quantum Chemistry*, 116(10):739–749, 2016. eprint: <https://onlinelibrary.wiley.com/doi/pdf/10.1002/qua.25096>.
 - [13] Alberto Castro, Miguel A. L. Marques, and Angel Rubio. Propagators for the time-dependent Kohn–Sham equations. *The Journal of Chemical Physics*, 121(8):3425–3433, August 2004.
 - [14] Adrián Gómez Pueyo, Miguel A. L. Marques, Angel Rubio, and Alberto Castro. Propagators for the Time-Dependent Kohn–Sham Equations: Multistep, Runge–Kutta, Exponential Runge–Kutta, and Commutator Free Magnus Methods. *Journal of Chemical Theory and Computation*, 14(6):3040–3052, June 2018. Publisher: American Chemical Society.
 - [15] Giuseppe Carleo, Ignacio Cirac, Kyle Cranmer, Laurent Daudet, Maria Schuld, Naftali Tishby, Leslie Vogt-Maranto, and Lenka Zdeborová. Machine learning and the physical sciences. *Reviews of Modern Physics*, 91(4):045002, December 2019. Publisher: American Physical Society.
 - [16] George Em Karniadakis, Ioannis G. Kevrekidis, Lu Lu, Paris Perdikaris, Sifan Wang, and Liu Yang. Physics-informed machine learning. *Nature Reviews Physics*, 3(6):422–440, June 2021.
 - [17] Nikola Kovachki, Zongyi Li, Burigede Liu, Kamyar Azizzadenesheli, Kaushik Bhattacharya, Andrew Stuart, and Anima Anandkumar. Neural Operator: Learning Maps Between Function Spaces With Applications to PDEs. *Journal of Machine Learning Research*, 24(89):1–97, 2023.
 - [18] Zongyi Li, Nikola Borislavov Kovachki, Kamyar Azizzadenesheli, Burigede Liu, Kaushik Bhattacharya, Andrew Stuart, and Anima Anandkumar. Fourier Neural Operator for Parametric Partial Differential Equations. In *International Conference on Learning Representations*, October 2020.
 - [19] Kamyar Azizzadenesheli, Nikola Kovachki, Zongyi Li, Miguel Liu-Schiaffini, Jean Kossaifi, and Anima Anandkumar. Neural operators for accelerating scientific simulations and design. *Nature Reviews Physics*, 6(5):320–328, May 2024. Publisher: Nature Publishing Group.
 - [20] John C. Snyder, Matthias Rupp, Katja Hansen, Klaus-Robert Müller, and Kieron Burke. Finding Density Functionals with Machine Learning. *Physical Review Letters*, 108(25):253002, June 2012. Publisher: American Physical Society.
 - [21] Felix Brockherde, Leslie Vogt, Li Li, Mark E. Tuckerman, Kieron Burke, and Klaus-Robert Müller. Bypassing the Kohn–Sham equations with machine learning. *Nature Communications*, 8(1):872, October 2017. Publisher: Nature Publishing Group.
 - [22] L. Fiedler, K. Shah, M. Bussmann, and A. Cangi. Deep dive into machine learning density functional theory for materials science and chemistry. *Physical Review Materials*, 6(4):040301, April 2022. Publisher: American Physical Society.
 - [23] Jun Yang and James Whitfield. Machine-learning Kohn–Sham potential from dynamics in time-dependent Kohn–Sham systems. *Machine Learning: Science and Technology*, 4(3):035022, August 2023. Publisher: IOP Publishing.
 - [24] Yasumitsu Suzuki, Ryo Nagai, and Jun Haruyama. Machine learning exchange-correlation potential in time-dependent density-functional theory. *Physical Review A*, 101(5):050501, May 2020. Publisher: American Physical Society.
 - [25] Logan Ward, Ben Blaiszik, Cheng-Wei Lee, Troy Martin, Ian Foster, and André Schleife. Accelerating Electronic Stopping Power Predictions by 10 Million Times with a Combination of Time-Dependent Density Functional Theory and Machine Learning, November 2023. arXiv:2311.00787 [cond-mat].
 - [26] Robert van Leeuwen. Causality and Symmetry in Time-Dependent Density-Functional Theory. *Physical Review Letters*, 80(6):1280–1283, February 1998. Publisher: American Physical Society.
 - [27] Carsten Ullrich. *Time-Dependent Density-Functional Theory: Concepts and Applications*. Oxford Graduate Texts. Oxford University Press, Oxford, New York, February 2012.
 - [28] J. Crank and P. Nicolson. A practical method for numerical evaluation of solutions of partial

- differential equations of the heat-conduction type. *Mathematical Proceedings of the Cambridge Philosophical Society*, 43(1):50–67, 1947.
- [29] Nicolas Tancogne-Dejean, Micael J. T. Oliveira, Xavier Andrade, Heiko Appel, Carlos H. Borca, Guillaume Le Breton, Florian Buchholz, Alberto Castro, Stefano Corni, Alfredo A. Correa, Umberto De Giovannini, Alain Delgado, Florian G. Eich, Johannes Flick, Gabriel Gil, Adrián Gomez, Nicole Helbig, Hannes Hübener, René Jestädt, Joaquim Jornet-Somoza, Ask H. Larsen, Irina V. Lebedeva, Martin Lüders, Miguel A. L. Marques, Sebastian T. Ohlmann, Silvio Pipolo, Markus Rampp, Carlo A. Rozzi, David A. Strubbe, Shunsuke A. Sato, Christian Schäfer, Iris Theophilou, Alicia Welden, and Angel Rubio. Octopus, a computational framework for exploring light-driven phenomena and quantum dynamics in extended and finite systems. *The Journal of Chemical Physics*, 152(12):124119, March 2020.
- [30] Lu Lu, Pengzhan Jin, and George Em Karniadakis. DeepONet: Learning nonlinear operators for identifying differential equations based on the universal approximation theorem of operators. *CoRR*, abs/1910.03193, 2019.
- [31] Anima Anandkumar, Kamyar Azizzadenesheli, Kaushik Bhattacharya, Nikola Kovachki, Zongyi Li, Burigede Liu, and Andrew Stuart. Neural Operator: Graph Kernel Network for Partial Differential Equations. In *ICLR 2020 Workshop on Integration of Deep Neural Models and Differential Equations*, February 2020.
- [32] J. Werschnik and E. K. U. Gross. Quantum optimal control theory. *Journal of Physics B: Atomic, Molecular and Optical Physics*, 40(18):R175, September 2007.

Appendix

4.1. Parameter Selection

This section outlines the parameters used in the simulations/calculations, derived from typical molecular properties and a literature review of relevant laser experiments.

Molecular Parameters The following ranges were considered for the 1D diatomic molecular model:

- **Bond Length (d):** 1 a.u. to 4 a.u.
- **Potential Well Depth (Z_i):** 1 a.u. to 4 a.u.

These ranges encompass typical values for diatomic molecules commonly studied in strong-field physics.

Laser Parameters Based on a literature review of typical laser experiments investigating molecular dynamics in strong fields, the following laser parameters were chosen:

- **Wavelength Range (λ):** 400 nm to 750 nm
 - Corresponding Photon Energy Range : 1.65 eV to 3.10 eV
- **Intensity Range (I):** 1.00×10^{12} to 5.00×10^{13} W cm $^{-2}$